
This manuscript is a preprint that has been accepted for publication in GEOLOGY before typesetting. The final version of this manuscript will be available via the 'Peer-reviewed Publication DOI' link on the right-hand side of this webpage. Please feel free to contact any of the authors; we welcome feedback.

1 Flexural strike-slip basins

2

3 **Derek Neuharth^{1,2}, Sascha Brune^{1,2}, Anne Glerum¹, Chris K. Morley³, Xiaoping Yuan^{1,4},**
4 **Jean Braun^{1,2}**

5 *¹GFZ German Research Centre for Geosciences, Telegrafenberg, 14473 Potsdam, Germany.*

6 *²Institute of Geosciences, University of Potsdam, Germany.*

7 *³PTTEP, Enco, Vibhavadi-Rangsit Road, Chatuchak, Bangkok, 10900, Thailand*

8 *⁴School of Earth Sciences, China University of Geosciences, Wuhan, China*

9

10 **ABSTRACT**

11 Strike-slip faults are classically associated with pull-apart basins where continental crust is thinned
12 between two laterally offset fault segments. Here we propose a subsidence mechanism to explain
13 the formation of a new type of basin where no substantial segment offset or syn-strike-slip thinning
14 is observed. Such “flexural strike-slip basins” form due to a sediment load creating
15 accommodation space by bending the lithosphere. We use a two-way coupling between the
16 geodynamic code ASPECT and surface processes code FastScape to show that flexural strike-slip
17 basins emerge if sediment is deposited on thin lithosphere close to a strike-slip fault. These
18 conditions were met at the Andaman Basin Central Fault, where seismic reflection data provide
19 evidence of a laterally extensive flexural basin with a depocenter located parallel to the strike-slip
20 fault trace.

21

22 **MOTIVATION**

23 Near plate boundaries, accommodation space for sedimentary basins is created by 1)
24 lithospheric stretching or cooling, which controls rift basin formation at divergent boundaries and
25 2) lithospheric flexure such as foreland basins in convergent settings and cratonic sag basins in
26 continental interiors (Allen and Allen, 2013). Pull-apart basins at transform plate boundaries are
27 thought to be related to the first process.

28 Pull-apart basins form between laterally offset strike-slip fault segments (Mann et al., 1983;
29 Gurbuz, 2010). During strike-slip motion, the area between the offset faults is extended and
30 basement subsidence in this area occurs due to crustal thinning (van Wijk et al., 2017). Pull-apart
31 basins lengthen over time and form as long thin basins with a depocenter that is bounded by the
32 strike- or oblique-slip segments (Seeber et al., 2004). While there are many pull-apart basin
33 examples (e.g., Dead Sea Basin, Garfunkel and Ben-Avraham, 1996; Death Valley Basin, SERPA
34 et al., 1988), there has not been much discussion on other types of strike-slip basins.

35 Flexural basins form when an overlying load deflects the lithosphere, for instance during
36 mountain building, where an orogenic load creates accommodation space for sediment infill.
37 However, under conditions without an orogenic load, basement subsidence may be a consequence
38 of lower crustal flow triggered by enhanced sedimentation in deep basins (Morley and Westaway,
39 2006; Clift et al., 2015), e.g. the fans of the Red (Clift and Sun, 2006) and Pearl Rivers (Dong et
40 al., 2020; both examples are located at the northern continental margin of the South China Sea).

41 We infer that the creation of sedimentation-induced accommodation space requires and is
42 enhanced by: 1) an easily deformable tectonic environment, and 2) focused sedimentation. Both
43 can occur in regions of prior tectonic subsidence. Furthermore, since strike-slip faults may

44 represent highly weakened plate boundaries (Zoback et al., 1987; Provost and Houston, 2003), and
45 transform continental margins often follow a phase of thinning (Jourdon et al., 2021), we formulate
46 the key hypothesis of this study: regions near strike-slip faults can represent a combination of
47 factors where significant basement subsidence is driven by sedimentary loading. The positive
48 feedback between focused sedimentation and flexural subsidence leads to the creation of a
49 previously unrecognized type of basin that we term “flexural strike-slip basin”. We test our
50 hypothesis by: 1) numerical forward modeling of a strike-slip system subjected to asymmetric
51 sedimentation, and 2) seismic reflection interpretation from the East Andaman Basin (EAB) in the
52 Andaman Sea.

53 **GEOLOGICAL SETTING OF THE ANDAMAN SEA**

54 During the Cenozoic, the Andaman Sea formed a transtensional backarc basin when India
55 coupled with western Myanmar (Curry, 2005). Multiple strike-slip faults exist in the region,
56 including the active, dextral, Sagaing Fault (Fig. 1; 18 mm/yr, Maurin et al., 2010; Vigny et al.,
57 2003) in the NE of the Andaman Sea that connects south-westward to the Andaman spreading
58 center (Curry, 2005). South of the Sagaing Fault is the inactive Andaman Basin Central (strike-
59 slip) Fault (ABCF; Morley, 2016, 2017; Mahattanachai et al., 2021).

60 The Andaman Sea’s transtensional motion led to subsidence and a submarine environment,
61 causing the area to act as a sediment trap. Fault trends suggest the region near the ABCF
62 experienced WNW-ESE extension in the Oligocene that shifted to NNW-SSE transtensional
63 strike-slip motion during the early to mid-Miocene (lasting ~5 Myr; Morley, 2017). The ABCF
64 follows a previous necking zone of hyperextended continental crust (7-10 km thick; Morley, 2017;
65 Mahattanachai et al., 2021), probably because mantle heterogeneities influenced the fault location
66 (Phillips et al., 2021). During strike-slip motion, the easterly Mergui Ridge (MR) was partially

67 subaerial and, along with peninsular Thailand acted as an asymmetric clastic sediment source for
68 the EAB located along the ABCF (Mahattanachai et al., 2021).

69 The geometry of the EAB in relation to the ABCF is described in detail by Mahattanachai
70 et al. (2021), who concluded that the long (>200 km), deep (>4 km), westward-thickening basin
71 on the east side of the sub-vertical ABCF did not fit classic extensional or pull-apart basin
72 characteristics.

73 **MODEL SETUP AND EVOLUTION**

74 We reproduce the key aspects of the ABCF region, namely that of a submarine
75 environment, thin lithosphere, and asymmetric sedimentation, using a viscoplastic $100 \times 8 \times 120$ km
76 (X, Y, Z) 3D box model via a two-way coupling of the tectonic code ASPECT (Fig. 2B,C;
77 Kronbichler et al., 2012; Heister et al., 2017; Glerum et al., 2018; Bangerth et al., 2019;
78 supplementary text S1) and the surface processes code FastScape (Braun and Willett, 2013; Yuan
79 et al., 2019a, 2019b; text S2). We assume that a previous extensional event left the region
80 submarine with thinned 40 km thick lithosphere. The model is initialized with 4 km upper crust, 4
81 km lower crust, 32 km mantle lithosphere, and 80 km of asthenosphere (Fig. 2B; Fig. S1). In Fig.
82 2B, the east boundary is no-slip in all directions, the west boundary is no-slip in the Z direction,
83 20 mm/yr in Y to induce strike-slip motion, and is given a small (0.2 mm/yr) extensional
84 component in X which helps avoid bending-induced compression but does not affect the presented
85 results (Fig. S2). The north and south boundaries are periodic to simulate an infinitely long strike-
86 slip fault with minimal along-strike variation, and the initial lithostatic pressure at a reference
87 location is prescribed on the bottom boundary to allow for outflow in response to sedimentation.
88 The strike-slip fault forms self-consistently above an initial perturbation of the Lithosphere-
89 Asthenosphere Boundary (10% of lithosphere thickness) in the center of the model that acts as a

90 weak zone for deformation to localize. Accumulated plastic strain weakens the angle of friction
91 over an interval of 0 to 1 from an initial value of 30° to a final value of 7.5° , promoting brittle
92 localization.

93 The surface processes code FastScape is coupled to the top of the tectonic model (text S3).
94 The model is submarine and transports sediment via diffusion with a coefficient of $500 \text{ m}^2/\text{yr}$,
95 consistent with open marine environments in previous modeling studies (Rouby et al., 2013).
96 Sediment is supplied to the domain in two ways: 1) The entire surface experiences 0.2 mm/yr of
97 pelagic/hemipelagic “sediment rain” sedimentation. 2) Ghost nodes (Fig. 2A) at the east boundary
98 are uplifted each timestep to prescribe a constant sediment flux of $40 \text{ m}^2/\text{yr}$, mimicking an off-
99 model sediment source similar to the MR for the EAB.

100 The models are run for 10 Myr, where the first 5 Myr represent the syn-tectonic stage with
101 strike-slip motion and sedimentation to mimic the ~ 5 Myr the ABCF was active. The final 5 Myr
102 constitute the post-tectonic stage with no prescribed motion or sediment supply, although sediment
103 transport continues (for setup details, see text S4).

104 **REFERENCE MODEL RESULTS**

105 In the reference model, strain localizes on a vertical fault near the model center (~ 0.5 Myr;
106 Fig. 2C). Both sides of the fault subside due to the influx of sediment, with the eastern side sinking
107 faster (1.0 vs. 0.4 mm/yr at 4.75 Myr). By 5 Myr, the eastern side has subsided more than the
108 western side (3.6 vs. 1.0 km), rotating the strike-slip fault to sub-vertical. After strike-slip motion
109 and sedimentation have ceased, the subsidence rate declines to 0.08 mm/yr as the sediment hill at
110 the eastern boundary is distributed across the surface. By 10 Myr, both sides have subsided another
111 0.4 km , showing a synformal thickening geometry along the fault.

112 The model indicates that a flexural strike-slip basin emerges due to sedimentation above
113 thin lithosphere close to a strike-slip fault, wherein the fault acts as a weak zone where subsidence
114 focuses. In contrast to classical half-grabens or pull-apart geometries, these basins form without a
115 significant extensional component (i.e., without crustal thinning).

116 To test controls on flexural strike-slip basin formation, we ran a series of models varying
117 in sedimentation rate, lithospheric thickness, and fault strength. Sedimentation rate was changed
118 by altering the eastern side influx from 0 (i.e., only sediment rain) to 60 m²/yr (Fig. 3A-D). With
119 no lateral input, both sides subsided evenly forming a synformal basin that is thickest at the fault
120 (Fig. 3A). This suggests that reference model basin asymmetry is primarily affected by
121 sedimentation, and not the initial perturbation. At higher lateral input, the eastern side subsided
122 more, from a maximum basement deflection of 0.9 km with no input to 5.7 km for 60 m²/yr of
123 input (Fig. 3D). The western side shows a less pronounced deflection with higher sediment input
124 (0.8 to 1.6 km), suggesting either that the sides are not fully decoupled or that more sediment
125 reached the western side.

126 The effects of varying the lithospheric thickness from 60 to 30 km (Fig. 3E-H) reduces the
127 basement flexural deflection on the eastern side of the fault from 4.6 km at 30 km to 1.4 km at 60
128 km, suggesting that deep flexural basins are unlikely to form in regions with thick lithosphere.

129 The final key variable is friction angle weakening (Fig. 3I-L). This shows that fault strength
130 affects flexural subsidence (4.2 vs. 3.3 km deflection at 99% and 25% weakening, respectively),
131 suggesting that regions with no weakening or without strike-slip motion (Fig. S3) would
132 experience much less subsidence. Further, weak faults promote lithospheric decoupling and basin
133 asymmetry related to asymmetric sedimentation.

134

135 **FLEXURAL STRIKE-SLIP BASINS IN THE ANDAMAN SEA**

136 Seismic data suggest the EAB as an asymmetric basin that spans both sides of the ABCF
137 (Mahattanachai et al., 2021). On the western side, basin thickness is fairly uniform (1-2 km; Fig.
138 1D). Along the fault on the eastern side the basin is substantially thicker (~5 km) and thins eastward
139 towards the sediment source areas of the MR and peninsular Thailand.

140 The Gulf of Moattama Basin (GMB) formed along the active Sagaing Fault, and is a more
141 ambiguous example where a deep (>10 km) depocenter formed in the last c. 6 Ma, although strike-
142 slip fault activity in the area probably dates to the Oligocene (Morley and Arboit, 2019). Although
143 a gentle releasing bend geometry is present in the offshore fault trace, the basin did not undergo
144 dramatic subsidence until the latest Miocene-Pliocene, when a major transgression followed
145 structural uplift and inversion of basins onshore (e.g., Morley and Alvey, 2015). We suggest the
146 axial sediment influx along the GMB resulted in the flexural strike-slip mechanism enhancing the
147 effects of the fault geometry.

148 The primary requirement for flexural strike-slip basin formation is weak or thin lithosphere
149 and high sedimentation rates. There are two basin types controlled by the sedimentation pattern:
150 1) symmetric, where both sides receive a similar sediment load (Fig. 3A) and, 2) asymmetric,
151 where the two distinct basin sides subside at different rates dependent on the sediment load they
152 receive (Fig. 3C). In both types, the maximum flexure and basin depocenter occur along the fault
153 trace, and the basin thins strike-perpendicularly.

154 The Andaman Sea provides likely examples for each flexural strike-slip basin type. 1) The
155 GMB, where northern axial sedimentation provided even sedimentation to each side of the fault

156 and formed a *symmetric flexural basin*. While sedimentation was not purely uniform, a synformal
157 geometry developed centered along the fault zone as in Fig. 3A. 2) The EAB (Fig. 1D), where
158 perpendicular sedimentation from the east forced greater flexure on the eastern side of the fault,
159 forming an *asymmetric flexural basin*. The EAB and reference model basin both have a change in
160 sediment thickness across the fault, and basin thinning toward the sediment source. Furthermore,
161 basin thicknesses (excluding post-tectonic sediment) along the fault's eastern side (4.5 vs. 5.2 km
162 in the model and EAB, respectively) and western side (1.8 vs. 1.3 km) are comparable.

163 Despite the similarities, there are discrepancies between the modeled basin and the EAB.
164 Eastward sediment thinning is less pronounced in the model. As the basement slope is affected by
165 the lithosphere thickness and sediment load, three possible explanations are: 1) The ABCF is
166 capped by a regional unconformity with the post-tectonic sediments (Morley, 2017; Srisuriyon and
167 Morley, 2014), and the fault may have received more sediment while active than expected from
168 the seismic data. 2) As the ABCF formed within a necking zone and the lithosphere thickness is
169 not well constrained, it may have varied spatially (rheologically or in thickness) and been thinner
170 than the 40 km value used here. 3) A more significant syn-strike-slip extensional component would
171 have further deepened the basin along the fault (Sobolev et al., 2005). Also, our models do not
172 consider basin translation with strike-slip motion. This is justified by comparison with the EAB,
173 where the thicker eastern basin is located on the same side as the MR and is not affected by the
174 translation. For the western basin, the ~350 km long MR is larger than the total dextral strike-slip
175 translation of ~90 km from the early to mid-Miocene.

176 Here we focused on the Andaman Sea, but the key requirements for flexural strike-slip
177 basins – thin lithosphere, focused sedimentation, and a weak fault – are possibly also met in the
178 New Guinea Basin in the Bismarck Sea (Fig. S4; Martinez and Taylor, 1996) and the Yinggehai

179 Basin in the South China Sea (Fig. S5; Clift and Sun, 2006), although new seismic data are needed
180 to test this. Another candidate is the Navassa Basin in the Jamaica Passage (Fig. S6; Corbeau et
181 al., 2016), an asymmetric strike-slip basin that is not located between offset segments. The basin
182 likely formed during strike-slip motion and does not contain older sedimentary units found in
183 nearby basins along the fault.

184 **CONCLUSION**

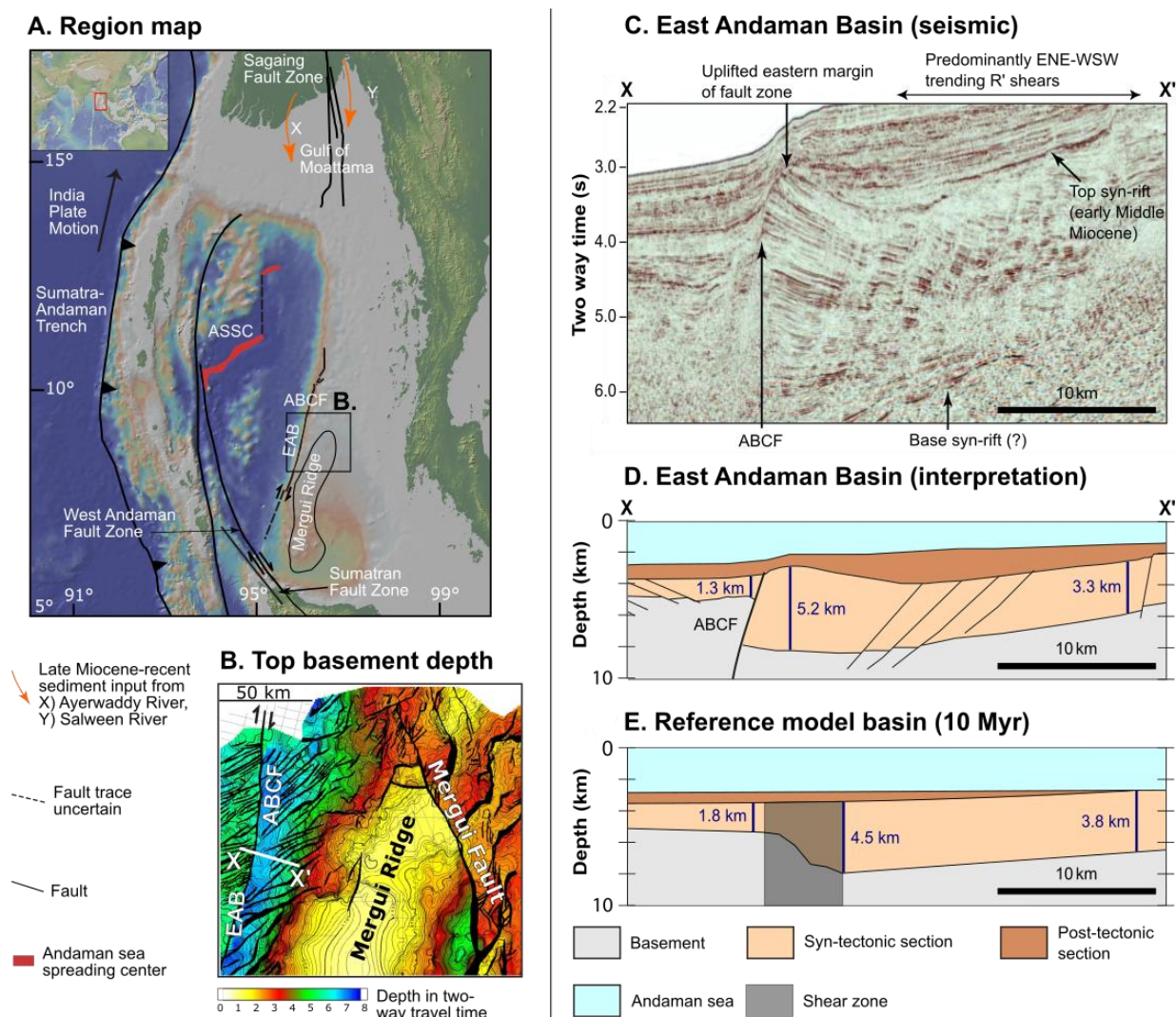
185 This study suggests a new class of flexural basins that form along strike-slip faults. These
186 basins are characterized by a fault-parallel depocenter and sediment that thins strike-
187 perpendicularly. The basins can be classified in two types, which are both represented in the
188 Andaman Sea: 1) *symmetric flexural basins*, where axial sedimentation causes a synformal shape,
189 as seen in the Gulf of Moattama Basin, and 2) *asymmetric flexural basins*, where asymmetric
190 sedimentation forces one basin side to subside more than the other, as seen in the East Andaman
191 Basin.

192 Flexural strike-slip basins form due to a strike-slip fault that acts as a weak zone facilitating
193 differential subsidence due to sediment loading. The fault decouples the lithosphere sides, allowing
194 them to respond independently to the sediment load they receive, determining basin symmetry.
195 For a flexural strike-slip basin to form, two criteria must be met: the strike-slip fault must 1) cut
196 through thin lithosphere and 2) be subjected to a sufficient tectonic load.

197 **ACKNOWLEDGMENTS**

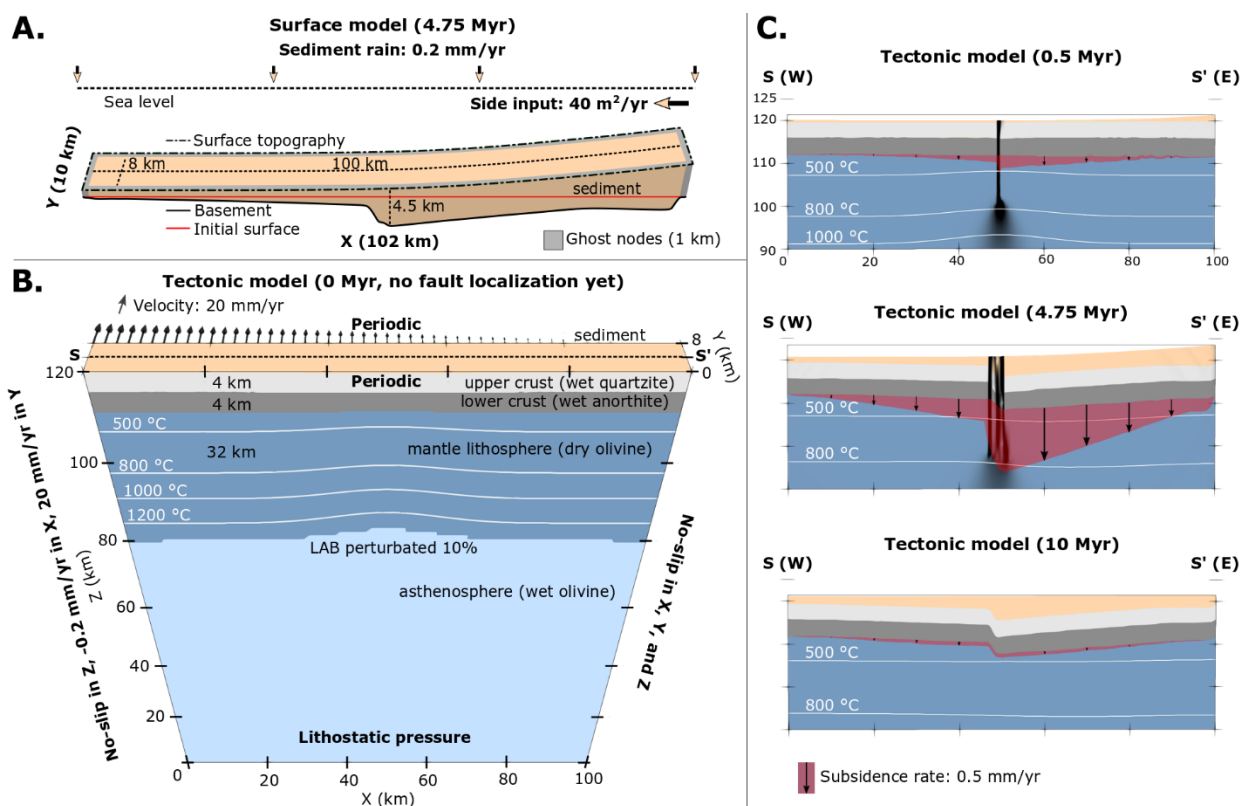
198 This study was conducted within the Helmholtz Young Investigators Group CRYSTALS
199 (VH-NG-1132). We thank the Computational Infrastructure for Geodynamics (geodynamics.org),
200 which is funded by the National Science Foundation under award EAR-0949446 and EAR-

201 1550901, for supporting the development of ASPECT. The work was supported by the North-
 202 German Supercomputing Alliance (HLRN). Software and input files are found at
 203 <http://doi.org/10.5281/zenodo.4893421>. Figures were made using ParaView, InkScape, and
 204 GeoMapApp. We thank PPTEP for providing the 2D seismic data. We also thank Anthony
 205 Jourdon, Zhen Sun, and an anonymous reviewer for their helpful reviews.



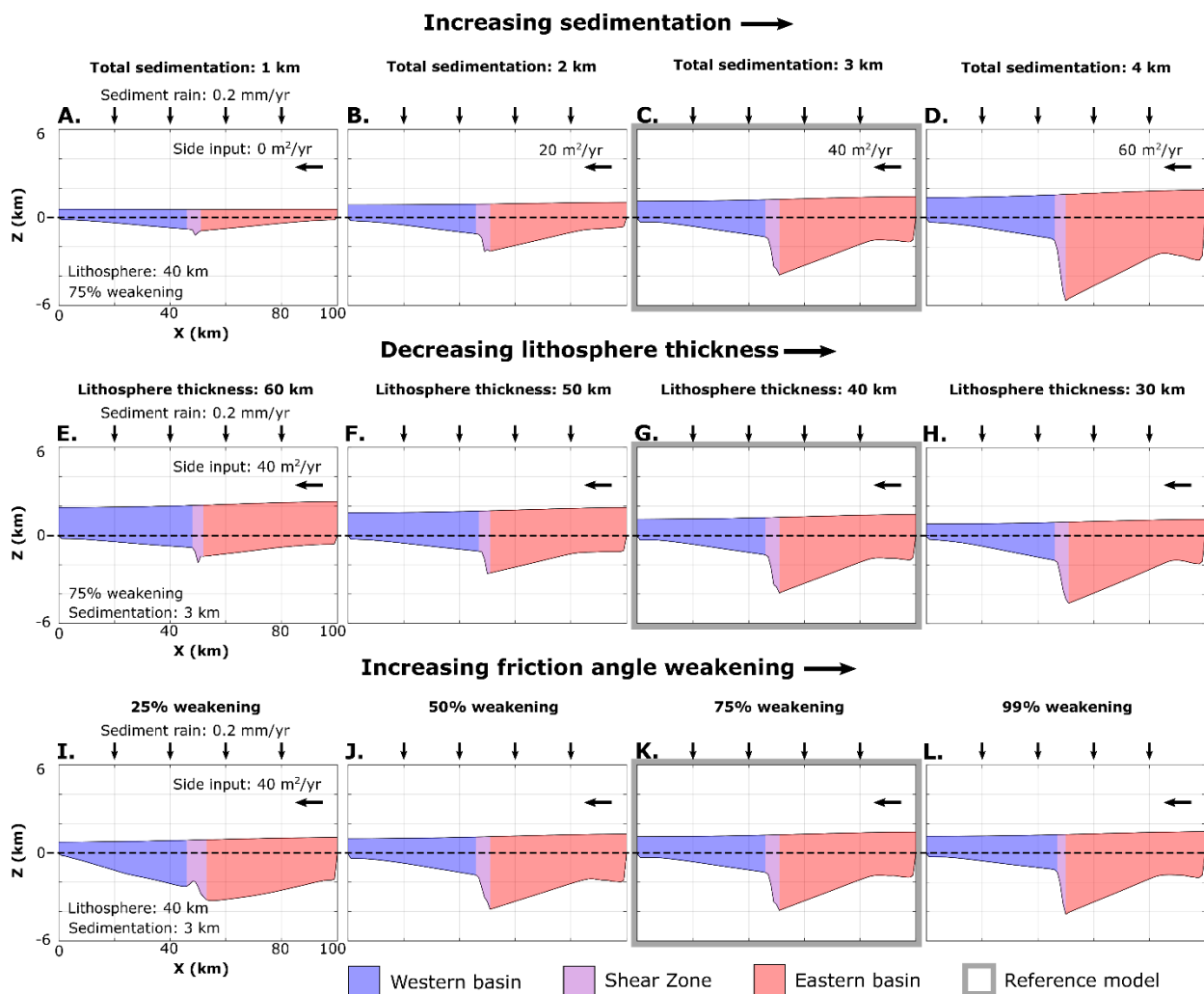
206
 207 **Figure 1. A. Andaman Sea Map. ASSC: Andaman Sea Spreading Center. ABCF:**
 208 **Andaman Basin Central Fault. EAB: East Andaman Basin. B. Depth to the top basement**
 209 **in two-way travel time. C. Seismic data of the EAB. D. Depth interpretation of C. E.**

210 **Modeled basin. Post-tectonic sediment is computed by adding the basement subsidence**
 211 **from 5 to 10 Myr to the topography at 5 Myr.**



212

213 **Figure 2. A. Surface processes model at 4.75 Myr and 2 times vertical exaggeration.**
 214 **Sediment (beige) is the area between the topography (dashed line) and basement (solid**
 215 **black line). Ghost nodes (gray), implemented for periodic advection along Y and to control**
 216 **the sedimentary side input, surround the surface model and do not interact with the**
 217 **tectonic model. B. Initial tectonic setup. Colors represent composition, white isotherms the**
 218 **temperature distribution. Arrows indicate the total velocity magnitude. LAB: Lithosphere-**
 219 **Asthenosphere Boundary. C. Cross-sections of the top 30 km of the tectonic model along S**
 220 **to S' in B showcase the formation of a flexural strike-slip basin in response to**
 221 **sedimentation. Subsidence rate at the Moho is indicated in red. See movies S1 and S2.**



222

223 **Figure 3. Basin formation when subject to variable sediment input (A-D), lithosphere**
 224 **thickness (E-H), and fault weakening (I-L). Dashed lines along Z=0 show the initial model**
 225 **elevation. Total sedimentation is the sediment thickness assuming even distribution across**
 226 **the model.**

227

228 **REFERENCES**

229 Allen, P.A., and Allen, J.R., 2013, Basin Analysis 3rd edition:,
 230 doi:10.1017/CBO9781107415324.004.

231 Bangerth, W., Dannberg, J., Gassmoeller, R., and Heister, T., 2019, ASPECT v2.1.0: Zenodo,

- 232 <https://doi.org/10.5281/zenodo.2653531>.
- 233 Braun, J., and Willett, S.D., 2013, A very efficient O(n), implicit and parallel method to solve the
234 stream power equation governing fluvial incision and landscape evolution: *Geomorphology*,
235 v. 180–181, p. 170–179, doi:10.1016/j.geomorph.2012.10.008.
- 236 Clift, P.D., Brune, S., and Quinteros, J., 2015, Climate changes control offshore crustal structure
237 at South China Sea continental margin: *Earth and Planetary Science Letters*, v. 420, p. 66–
238 72, doi:10.1016/j.epsl.2015.03.032.
- 239 Clift, P.D., and Sun, Z., 2006, The sedimentary and tectonic evolution of the Yinggehai-Song
240 Hong basin and the southern Hainan margin, South China Sea: Implications for Tibetan
241 uplift and monsoon intensification: *Journal of Geophysical Research: Solid Earth*, v. 111, p.
242 1–28, doi:10.1029/2005JB004048.
- 243 Corbeau, J., Rolandone, F., Leroy, S., Mercier de Lépinay, B., Meyer, B., Ellouz-Zimmermann,
244 N., and Momplaisir, R., 2016, The northern Caribbean plate boundary in the Jamaica
245 Passage: Structure and seismic stratigraphy: *Tectonophysics*, v. 675, p. 209–226,
246 doi:10.1016/j.tecto.2016.03.022.
- 247 Curray, J.R., 2005, Tectonics and history of the Andaman Sea region: *Journal of Asian Earth
248 Sciences*, v. 25, p. 187–232, doi:10.1016/j.jseaes.2004.09.001.
- 249 Dong, M., Zhang, J., Brune, S., Wu, S., Fang, G., and Yu, L., 2020, Quantifying Postrift Lower
250 Crustal Flow in the Northern Margin of the South China Sea: *Journal of Geophysical
251 Research: Solid Earth*, v. 125, doi:10.1029/2019JB018910.
- 252 Garfunkel, Z., and Ben-Avraham, Z., 1996, The structure of the Dead Sea basin: *Tectonophysics*,
253 v. 266, p. 155–176, doi:10.1016/S0040-1951(96)00188-6.
- 254 Glerum, A., Thieulot, C., Fraters, M., Blom, C., and Spakman, W., 2018, Nonlinear
255 viscoplasticity in ASPECT: Benchmarking and applications to subduction: *Solid Earth*, v. 9,
256 p. 267–294, doi:10.5194/se-9-267-2018.
- 257 Gurbuz, A., 2010, Geometric characteristics of pull-apart basins: *Lithosphere*, v. 2, p. 199–206,
258 doi:10.1130/L36.1.
- 259 Heister, T., Dannberg, J., Gassmöller, R., and Bangerth, W., 2017, High Accuracy Mantle
260 Convection Simulation through Modern Numerical Methods – II: Realistic Models and
261 Problems.: *Geophysical Journal International*, v. 210, p. 833–851,
262 doi:doi:10.1093/gji/ggx195.
- 263 Jourdon, A., Kergaravat, C., Duclaux, G., and Huguen, C., 2021, Looking beyond kinematics:
264 3D thermo-mechanical modelling reveals the dynamics of transform margins: *Solid Earth*,
265 v. 12, p. 1211–1232, doi:10.5194/se-12-1211-2021.
- 266 Kronbichler, M., Heister, T., and Bangerth, W., 2012, High Accuracy Mantle Convection
267 Simulation through Modern Numerical Methods.: *Geophysical Journal International*, v. 191,
268 doi:doi:10.1111/j.1365-246x.2012.05609.x.
- 269 Mahattanachai, T., Morley, C.K., Charusiri, P., and Kanjanapayont, P., 2021, The Andaman
270 Basin Central Fault Zone, Andaman Sea: Characteristics of a major deepwater strike-slip

- 271 fault system in a polyphase rift: *Marine and Petroleum Geology*, p. 104997,
272 doi:10.1016/j.marpetgeo.2021.104997.
- 273 Mann, P., Hempton, M.R., Dwight, C.B., and Burke, K., 1983, Development of Pull-Apart
274 Basins Authors: Paul Mann , Mark R . Hempton , Dwight C . Bradley and Kevin Burke
275 Published by : The University of Chicago Press Stable URL :
276 <http://www.jstor.org/stable/30064017> . All use subject to JSTOR Terms and Conditio: The
277 *Journal of Geology*, v. 91, p. 529–554.
- 278 Martinez, F., and Taylor, B., 1996, Backarc spreading, rifting, and microplate rotation, between
279 transform faults in the Manus Basin: *Marine Geophysical Researches*, v. 18, p. 203–224,
280 doi:10.1007/BF00286078.
- 281 Maurin, T., Masson, F., Rangin, C., Min, U.T., and Collard, P., 2010, First global positioning
282 system results in northern Myanmar: Constant and localized slip rate along the Sagaing
283 fault: *Geology*, v. 38, p. 591–594, doi:10.1130/G30872.1.
- 284 Morley, C.K., 2017, Cenozoic rifting, passive margin development and strike-slip faulting in the
285 Andaman Sea: A discussion of established v. New tectonic models: *Geological Society
286 Memoir*, v. 47, p. 27–50, doi:10.1144/M47.4.
- 287 Morley, C.K., 2016, The impact of multiple extension events, stress rotation and inherited fabrics
288 on normal fault geometries and evolution in the Cenozoic rift basins of Thailand:
289 *Geological Society, London, Special Publications*, v. 439, p. 413–445,
290 doi:<https://doi.org/10.1144/SP439.3>.
- 291 Morley, C.K., and Alvey, A., 2015, Is spreading prolonged, episodic or incipient in the Andaman
292 Sea? Evidence from deepwater sedimentation: *Journal of Asian Earth Sciences*, v. 98, p.
293 446–456, doi:10.1016/j.jseaes.2014.11.033.
- 294 Morley, C.K., and Arboit, F., 2019, Dating the onset of motion on the Sagaing fault: Evidence
295 from detrital zircon and titanite U-Pb geochronology from the North Minwun Basin,
296 Myanmar: *Geology*, v. 47, p. 581–585, doi:10.1130/G46321.1.
- 297 Morley, C.K., and Westaway, R., 2006, Subsidence in the super-deep Pattani and Malay basins
298 of Southeast Asia: A coupled model incorporating lower-crustal flow in response to post-rift
299 sediment loading: *Basin Research*, v. 18, p. 51–84, doi:10.1111/j.1365-2117.2006.00285.x.
- 300 Phillips, T.B., Naliboff, J.B., Mccaffrey, K.J.W., Pan, S., and van Hunen, J., 2021, The influence
301 of crustal strength on rift geometry and development - Insights from 3D numerical
302 modelling: [preprint], doi:<https://doi.org/10.31223/X58K61>.
- 303 Provost, A.-S., and Houston, H., 2003, Stress orientations in northern and central California:
304 Evidence for the evolution of frictional strength along the San Andreas plate boundary
305 system: *Journal of Geophysical Research: Solid Earth*, v. 108, p. 1–18,
306 doi:10.1029/2001jb001123.
- 307 Rouby, D., Braun, J., Robin, C., Dauteuil, O., and Deschamps, F., 2013, Long-term stratigraphic
308 evolution of Atlantic-type passive margins: A numerical approach of interactions between
309 surface processes, flexural isostasy and 3D thermal subsidence: *Tectonophysics*, v. 604, p.
310 83–103, doi:10.1016/j.tecto.2013.02.003.

- 311 Seeber, L., Emre, O., Cormier, M.H., Sorlien, C.C., McHugh, C.M.G., Polonia, A., Ozer, N., and
312 Cagatay, N., 2004, Uplift and subsidence from oblique slip: The Ganos-Marmara bend of
313 the North Anatolian Transform, Western Turkey: *Tectonophysics*, v. 391, p. 239–258,
314 doi:10.1016/j.tecto.2004.07.015.
- 315 SERPA, L., DE VOOGD, B., WRIGHT, L., WILLEMIN, J., OLIVER, J., HAUSER, E., and
316 TROXEL, B., 1988, Structure of the central Death Valley pull-apart basin and vicinity from
317 COCORP profiles in the southern Great Basin: *GSA Bulletin*, v. 100, p. 1437–1450,
318 doi:10.1130/0016-7606(1988)100<1437:SOTCDV>2.3.CO;2.
- 319 Sobolev, S. V., Petrunin, A., Garfunkel, Z., and Babeyko, A.Y., 2005, Thermo-mechanical
320 model of the Dead Sea Transform: *Earth and Planetary Science Letters*, v. 238, p. 78–95,
321 doi:10.1016/j.epsl.2005.06.058.
- 322 Srisuriyon, K., and Morley, C.K., 2014, Pull-apart development at overlapping fault tips:
323 Oblique rifting of a Cenozoic continental margin, northern Mergui Basin, Andaman Sea:
324 *Geosphere*, v. 10, p. 80–106, doi:10.1130/GES00926.1.
- 325 Vigny, C., Socquet, A., Rangin, C., Chamot-Rooke, N., Pubellier, M., Bouin, M.-N., Bertrand,
326 G., and Becker, M., 2003, Present-day crustal deformation around Sagaing fault, Myanmar:
327 *Journal of Geophysical Research: Solid Earth*, v. 108,
328 doi:https://doi.org/10.1029/2002JB001999.
- 329 van Wijk, J., Axen, G., and Abera, R., 2017, Initiation, evolution and extinction of pull-apart
330 basins: Implications for opening of the Gulf of California: *Tectonophysics*, v. 719–720, p.
331 37–50, doi:10.1016/j.tecto.2017.04.019.
- 332 Yuan, X.P., Braun, J., Guerit, L., Rouby, D., and Cordonnier, G., 2019a, A New Efficient
333 Method to Solve the Stream Power Law Model Taking Into Account Sediment Deposition:
334 *Journal of Geophysical Research: Earth Surface*, v. 124, p. 1346–1365,
335 doi:10.1029/2018JF004867.
- 336 Yuan, X.P., Braun, J., Guerit, L., Simon, B., Bovy, B., Rouby, D., Robin, C., and Jiao, R.,
337 2019b, Linking continental erosion to marine sediment transport and deposition: A new
338 implicit and O(N) method for inverse analysis: *Earth and Planetary Science Letters*, v. 524,
339 p. 115728, doi:10.1016/j.epsl.2019.115728.
- 340 Zoback, M.D. et al., 1987, New evidence on the state of stress of the san andreas fault system:
341 *Science*, v. 238, p. 1105–1111, doi:10.1126/science.238.4830.1105.
- 342

1 Supplementary Information

2 Flexural strike-slip basins

3
4 **Derek Neuharth^{1,2}, Sascha Brune^{1,2}, Anne Glerum¹, Chris K. Morley³, Xiaoping Yuan^{1,4},**
5 **Jean Braun^{1,2}**
6

7 ¹GFZ German Research Centre for Geosciences, Telegrafenberg, 14473 Potsdam, Germany.

8 ²Institute of Geosciences, University of Potsdam, Germany.

9 ³PTTEP, Enco, Vibhavadi-Rangsit Road, Chatuchak, Bangkok, 10900, Thailand

10 ⁴School of Earth Sciences, China University of Geosciences, Wuhan, China

11

12 **Contents of this file**

13 Text S1 – ASPECT methods

14 Text S2 – FastScape methods

15 Text S3 – ASPECT/FastScape coupling

16 Text S4 – Model setup

17 Table S1

18 Table S2

19 Figure S1

20 Figure S2

21 Figure S3

22 Figure S4

23 Figure S5

24 Figure S6

25

26 **Additional supporting information (uploaded separately)**

27 Video S1

28 Video S2

29

30 **Text S1: ASPECT Methods**

31 **1.1 Governing equations**

32 We perform numerical simulations of a 3D strike-slip system using the open source finite-element
 33 code ASPECT (Advanced Solver for Problems in Earth's ConvecTion, version 2.3.0-pre, commit
 34 886749d; Heister et al., 2017; Kronbichler et al., 2012; Rose et al., 2017; Bangerth et al., 2019).
 35 ASPECT solves the following incompressible conservation equations assuming an infinite Prandtl
 36 number (i.e., without the inertial term),

37
$$-\nabla \cdot (2\eta\dot{\epsilon}) + \nabla P = \rho \mathbf{g}, \quad (1)$$

38
$$\nabla \cdot (\mathbf{u}) = 0, \quad (2)$$

39
$$\bar{\rho} C_p \left(\frac{\partial T}{\partial t} + \mathbf{u} \cdot \nabla T \right) - \nabla \cdot \mathbf{k} \nabla T = \bar{\rho} H \quad (3)$$

40
$$+ \alpha T (\mathbf{u} \cdot \nabla P),$$

41
$$\frac{\partial c_i}{\partial t} + \mathbf{u} \cdot \nabla c_i = q_i, \quad (4)$$

42 where equation (1) represents the conservation of momentum, with η the effective viscosity, $\dot{\epsilon}$ the
 43 deviator of the strain rate tensor (defined as $\frac{1}{2}(\nabla \mathbf{u} + (\nabla \mathbf{u})^T)$), \mathbf{u} the velocity, P the pressure, ρ the
 44 density, and \mathbf{g} gravity. Equation (2) describes the conservation of volume. Equation (3) represents
 45 the conservation of energy where $\bar{\rho}$ is the reference adiabatic density, C_p the specific heat capacity,
 46 T the temperature, \mathbf{k} the thermal conductivity, H the radiogenic heating, and α the thermal
 47 expansivity. As right-hand-side heating terms, we include radioactive heating and adiabatic
 48 heating, in that order. Finally, we solve the advection equation (4) for each compositional field c_i
 49 (e.g., upper crust, lower crust, and accumulated plastic strain) with reaction rate q_i nonzero only
 50 for the plastic strain field.

51 1.2 Rheology

52 We use a visco-plastic rheology (Glerum et al., 2018), which additionally includes plastic
53 weakening based on accumulated plastic strain. In the viscous regime, we use a composite of
54 diffusion and dislocation creep (Karato and Wu, 1993), formulated as:

$$55 \quad \eta_{\text{eff}}^{\text{diff|dis}} = \frac{1}{2} A_{\text{diff|dis}}^{-1} d^m \dot{\epsilon}_e^{\frac{1-n}{n}} \exp\left(\frac{(E_{\text{diff|dis}} + PV_{\text{diff|dis}})}{nRT}\right), \quad (5)$$

56 where A is a scalar prefactor, d the grain size, $\dot{\epsilon}_e$ the square root of second invariant of the
57 deviatoric strain rate, E the activation energy, P the pressure, V the activation volume, R the gas
58 constant, T the temperature, and n the stress exponent. For diffusion, $n = 1$ and the equation
59 becomes independent of strain rate. For dislocation creep, the grain size exponent m vanishes,
60 rendering dislocation creep independent of grain size. Values for A , E , V , and n used in our models
61 are composition-dependent and can be found in supplementary Table S1.

62 In the plastic regime, when viscous stresses exceed the yield stress, we use the Drucker-Prager
63 yield criterion (Davis and Selvadurai, 2002). The effective plastic viscosity is given by

$$64 \quad \eta_{\text{eff}}^{\text{pl}} = \frac{\frac{6C \cos\phi}{\sqrt{3}(3-\sin\phi)} + \frac{6P \sin\phi}{\sqrt{3}(3-\sin\phi)}}{2\dot{\epsilon}_e}, \quad (6)$$

65 where C is the cohesion and ϕ the internal angle of friction. The accumulation of plastic strain is
66 tracked as a compositional field. This field is used to linearly weaken ϕ from an initial value of
67 30° to a final value of 7.5° over the accumulated plastic strain interval of 0 to 1. The time-integrated
68 value of the strain reaction rate q_i is approximated as $\dot{\epsilon}_e \cdot dt$ when plastic yielding occurs (with dt
69 the current timestep size).

70 **Text S2: FastScape Methods**

71 FastScape is a landscape evolution code that changes the topographic surface through uplift,
 72 advection, the stream-power law, and hillslope diffusion (Braun and Willett, 2013). It can
 73 additionally deposit fluvial sediment (Yuan et al., 2019a) and include a marine component, which
 74 handles marine sediment (sand/silt) transport and deposition, and layer compaction based on
 75 sand/silt porosity (Yuan et al., 2019b). It uses a 2D horizontal mesh with a uniform resolution. For
 76 simplicity, we here assume that the entire model surface is submarine, with uniform properties
 77 (i.e., sand and silt transport coefficients are the same), and that there is no compaction (porosity is
 78 zero). Hence, FastScape deforms the surface through the uplift rate and marine diffusion equation
 79 only as

$$80 \quad \frac{dh}{dt} = \mathbf{U} + K_m \nabla^2 h, \quad (7)$$

81 where h is the topographic elevation, \mathbf{U} the uplift rate and K_m the marine sediment diffusion
 82 coefficient.

83 **Text S3: ASPECT/FastScape coupling**

84 In this paper we use a two-way coupling of the tectonic ASPECT code and the landscape evolution
 85 FastScape code. For this coupling, a FastScape shared library is called by an ASPECT plugin to
 86 deform its surface as described in the previous section. The plugin has three main components: 1)
 87 Copy the surface height and velocity values from ASPECT. 2) Initialize and run FastScape at a
 88 resolution equivalent to or greater than the one used at the surface of ASPECT. If it is the first
 89 timestep of the tectonic model run, FastScape is initialized using height and velocity values from
 90 ASPECT. In subsequent timesteps, as FastScape runs separately and can be at a higher resolution
 91 than ASPECT, only the velocity values from ASPECT are transferred to FastScape. Before

92 running FastScape, the initial topography values are saved. After running FastScape, the new and
93 previous topography are compared to determine a nodal vertical (Z) velocity,

$$94 \quad \mathbf{V}_z = \frac{h_c - h_p}{dt_a}, \quad (8)$$

95 where h_p is the surface height at the start of the timestep (previous surface), and h_f the surface
96 height after FastScape has been run (current surface), and dt_a the ASPECT timestep. 3) Using the
97 overarching mesh deformation functionality (see Rose et al., 2017), the Z velocity field is
98 interpolated onto the ASPECT surface to determine the displacement of the mesh surface and
99 interior. From there, ASPECT responds to the change in topography calculated by FastScape due
100 to the induced change in forces that is included in the Stokes equations. At the beginning of the
101 next timestep, the updated velocities computed in the previous timestep are sent to FastScape once
102 again.

103 The FastScape mesh includes an additional element-size layer of ghost nodes compared to the
104 ASPECT surface mesh. The values of surface height on these nodes are not considered when
105 interpolating the surface back to ASPECT and are used primarily to avoid FastScape boundary
106 artifacts being sent to the ASPECT model (e.g., the boundaries do not uplift from advected
107 topography). To avoid possible erroneous sediment flux out or into the model from artificial
108 slopes, each timestep the ghost nodes are updated with the topography and velocity values of the
109 nearest inward node (an ASPECT boundary node).

110 Besides passing ASPECT's uplift velocities, we use the plugin's FastScape interface to supply
111 additional input to the surface process model in two ways: 1) to add marine background
112 sedimentation via the sediment rain effect, and 2) to add a boundary sediment flux using the ghost
113 nodes. For the sediment rain, at each nodal point we update FastScape with a flat height increase

114 every ASPECT timestep. Through the diffusion component in equation (7), we prescribe a constant
115 sediment flux at the boundary, assuming that

$$116 \quad \mathbf{Q} = K_m S, \quad (9)$$

117 where \mathbf{Q} is the sediment flux and S the slope. Since K_m and Q are user-set parameters, to achieve
118 this we alter S by uplifting the boundary ghost nodes every ASPECT timestep so that \mathbf{Q} remains
119 constant.

120 **Text S4: Model setup**

121 In this study we examine how a strike-slip fault responds to sedimentation. We therefore set up a
122 3D box model with dimensions 100×8×120 km (X , Y , and Z , where Z is the vertical component)
123 and 5 compositions representing a wet quartzite upper crust (Rutter and Brodie, 2004), wet
124 anorthite lower crust (Rybacki et al., 2006), dry olivine lithospheric mantle, wet olivine
125 asthenosphere (Hirth and Kohlstedt, 2003), and a sediment layer that has rheologic parameters
126 identical to wet quartzite, but with density and temperature parameters consistent with sediment
127 (Sippel et al., 2017). The total crustal thickness is set to 8 km (4 km upper crust, 4 km lower crust)
128 based on crustal estimates of the area (7-10 km; Mahattanachai et al., 2021). The lithospheric
129 mantle extends between the Moho and the lithosphere-asthenosphere boundary (LAB) at 40 km
130 depth. The LAB depth, like the crust, has been perturbed by a previous extensional period. The
131 remaining material beneath the LAB is considered asthenosphere (Fig. S1). While there is no initial
132 sediment layer, the top boundary is fixed to a sediment composition so that any top-inflow of
133 material due to topography changes other than uplift is sediment.

134 The ASPECT model mesh consists of two element sizes: 1 km and 2 km. The upper 8 km of the
135 model is refined at 1 km to best resolve the crust and the forming sediment layer. This high-

136 resolution area additionally extends to a depth of 35 k from $X = 42$ km to $X = 52$ km to better
137 resolve the strike-slip fault. All other areas are kept at 2 km resolution.

138 The initial temperature above the LAB is determined by a steady-state geotherm (Turcotte and
139 Schubert, 2013), and below by a mantle adiabat. For simplicity, an initial weak zone is seeded
140 through a small perturbation: we raise the LAB locally by 10% of the lithospheric mantle thickness.
141 We fix the top boundary temperature at 0 °C and the bottom boundary at the temperature initially
142 determined from the mantle adiabat at that depth. All other boundaries are set to zero heat-flux.

143 The coupled model is run for 10 Myr, where the model in the first 5 Myr includes non-zero velocity
144 boundary conditions. During this time, the western boundary is given a strike-slip component of
145 20 mm/yr (in Y), and an extensional component of 0.2 mm/yr (in X), while the Z-component of
146 velocity is set to no-slip. This gives a total of 100 km of dextral strike-slip motion and 1 km of
147 extension. The small extensional component is introduced to avoid compressional pop-ups that
148 form at the shear zone as the lithosphere subsides due to the sediment load (Fig. S2). The exact
149 extensional value is chosen to accommodate horizontal stress forces related to isostatic
150 compensation. From 5-10 Myr, extension and strike-slip motion stop as the western boundary is
151 set to no-slip in all directions. All other boundary conditions are constant for the entire model run,
152 with the eastern boundary being no-slip in all directions, the north and south boundaries set to
153 periodic to simulate an infinitely long strike-slip fault, the initial lithostatic pressure computed at
154 a reference location prescribed on the bottom boundary to allow for outflow in response to
155 sedimentation, and the top boundary deformed through the use of FastScape.

156 FastScape is set up with an arbitrarily high sea level so that the entire model is considered
157 submarine. This setup leads to a model with no acting stream power law, and sediment being
158 moved solely through marine sediment diffusion. For simplicity, we additionally assume that there

159 is no compaction and no difference between sand and silt. As such, we use a diffusion coefficient
160 of $500 \text{ m}^2/\text{y}$ for both, a value consistent with open marine environments in previous modelling
161 studies (e.g., Rouby et al., 2013). During the syn-strike-slip phase of the tectonic model (0-5 Myr)
162 we supply sediment to the model in two ways: 1) To account for pelagic/hemipelagic
163 sedimentation (sediment rain), we deposit at a constant and uniform sedimentation rate of 0.2
164 mm/yr. 2) We assume there is an asymmetric off-model source of sediment, similar to the eastern
165 Mergui Ridge for the East Andaman Basin, that inputs sediment into the system from the eastern
166 boundary at a rate of $40 \text{ m}^2/\text{yr}$. This is done through equation (9), wherein we uplift the ghost nodes
167 at each timestep so that a constant flux is prescribed through marine diffusion. After this syn-
168 tectonic stage spanning 5 Myr, sediment supply to the system is halted, although marine diffusion
169 continues to work on the topography.

170

Parameter	Symbol	Units	Sediment	Upper crust	Lower crust	Lithospheric mantle	Asthenosphere
Reference density (at surface conditions)	ρ_0	kg m ⁻³	2520	2700	2850	3280	3300
Thermal expansivity	α	K ⁻¹	$3.7 \cdot 10^{-5}$	$2.7 \cdot 10^{-5}$	$2.7 \cdot 10^{-5}$	$3.0 \cdot 10^{-5}$	$3.0 \cdot 10^{-5}$
Thermal diffusivity	κ	m ² s ⁻¹	$7.28 \cdot 10^{-7}$	$9.26 \cdot 10^{-7}$	$5.85 \cdot 10^{-7}$	$8.38 \cdot 10^{-7}$	$8.33 \cdot 10^{-7}$
Heat capacity	C_p	J kg ⁻¹ K ⁻¹	1200	1200	1200	1200	1200
Heat production	H	W m ⁻³	$1.2 \cdot 10^{-6}$	$1.5 \cdot 10^{-6}$	$0.2 \cdot 10^{-6}$	0	0
Cohesion	C	Pa	$20 \cdot 10^6$	$20 \cdot 10^6$	$20 \cdot 10^6$	$20 \cdot 10^6$	$20 \cdot 10^6$
Internal friction angle (unweakened)	ϕ	°	30	30	30	30	30
Strain weakening interval	-	-	[0,1]	[0,1]	[0,1]	[0,1]	[0,1]
Strain weakening factor	ϕ_{wf}	-	0.25	0.25	0.25	0.25	0.25
Creep properties			Sediment	Wet quartzite	Wet anorthite	Dry olivine	Wet olivine
Stress exponent (dis)	n	-	4.0	4.0	3.0	3.5	3.5
Constant prefactor (dis)	A_{dis}	Pa ⁻ⁿ s ⁻¹	$8.57 \cdot 10^{-28}$	$8.57 \cdot 10^{-28}$	$7.13 \cdot 10^{-18}$	$6.52 \cdot 10^{-16}$	$2.12 \cdot 10^{-15}$
Activation energy (dis)	E_{dis}	J mol ⁻¹	$223 \cdot 10^3$	$223 \cdot 10^3$	$345 \cdot 10^3$	$530 \cdot 10^3$	$480 \cdot 10^3$
Activation volume (dis)	V_{dis}	m ³ mol ⁻¹	0	0	$38 \cdot 10^{-6}$	$18 \cdot 10^{-6}$	$11 \cdot 10^{-6}$
Constant prefactor (diff)	A_{diff}	Pa ⁻¹ s ⁻¹	$5.79 \cdot 10^{-19}$	$5.79 \cdot 10^{-19}$	$2.99 \cdot 10^{-25}$	$2.25 \cdot 10^{-9}$	$1.5 \cdot 10^{-9}$
Activation energy (diff)	E_{diff}	J mol ⁻¹	$223 \cdot 10^3$	$223 \cdot 10^3$	$159 \cdot 10^3$	$375 \cdot 10^3$	$335 \cdot 10^3$
Activation volume (diff)	V_{diff}	m ³ mol ⁻¹	0	0	$38 \cdot 10^{-6}$	$6 \cdot 10^{-6}$	$4 \cdot 10^{-6}$
Grain size (diff)	d	m	0.001	0.001	0.001	0.001	0.001
Grain size exponent (diff)	m	-	2.0	2.0	3.0	0	0

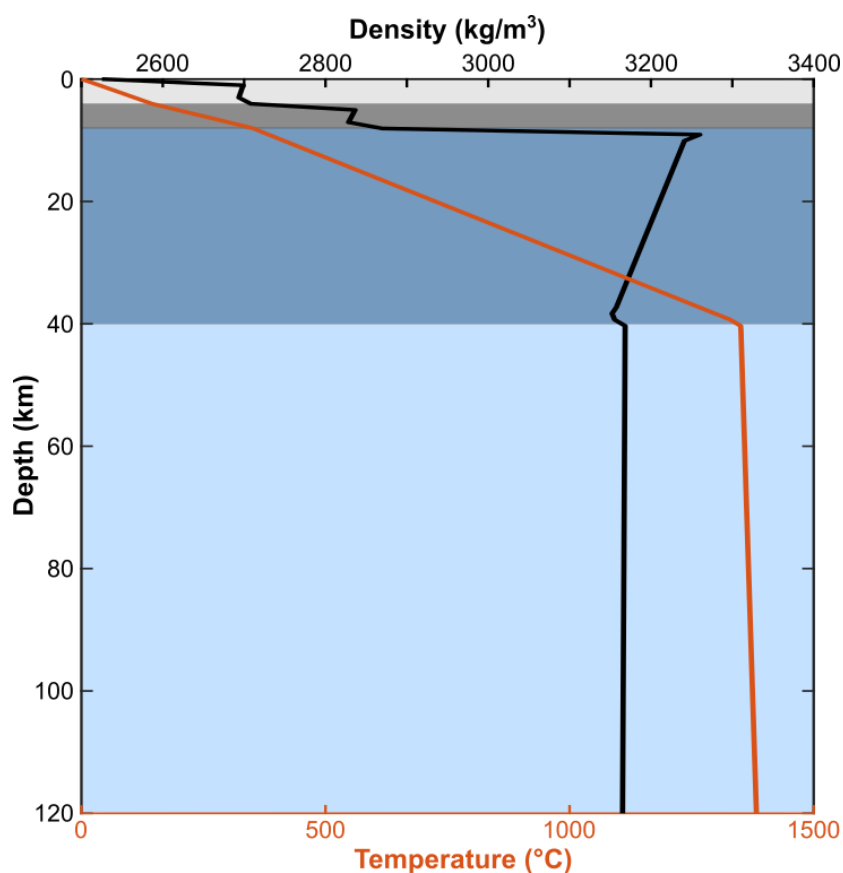
171 **Table S1:** ASPECT model parameters. Abbreviations: dis – dislocation creep, diff – diffusion
172 creep.

173

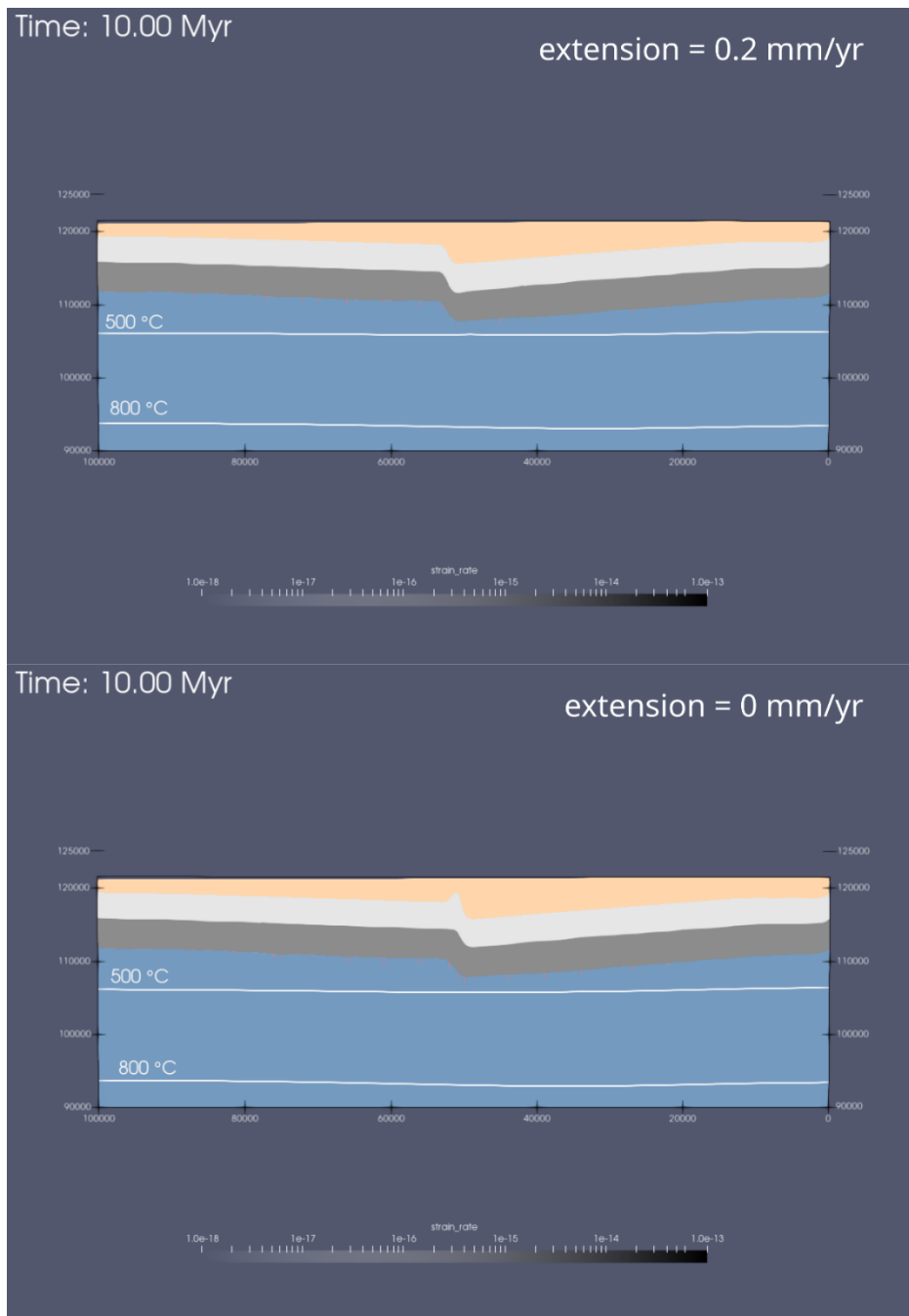
Parameter	Symbol	Unit	Value
Marine sand transport coefficient	K_{sand}	m^2/yr	500
Surface sand porosity	φ_{sand}	-	0
Sand e-folding depth	z_{sand}	m	0
Marine silt transport coefficient	K_{silt}	m^2/yr	500
Surface silt porosity	φ_{silt}	-	0
Silt e-folding depth	z_{silt}	m	0
Sand-shale ratio	F	-	1
Thickness of transport layer	L	m	100
Sea level	h_{sea}	m	5000

174 **Table S2:** FastScape model parameters.

175



176 **Figure S1:** Initial density (black) and temperature (red) profiles with depth. Colored backgrounds
 177 represent the initial compositions, with light gray representing the upper crust, dark gray the lower
 178 crust, dark blue the mantle lithosphere, and light blue the asthenosphere.



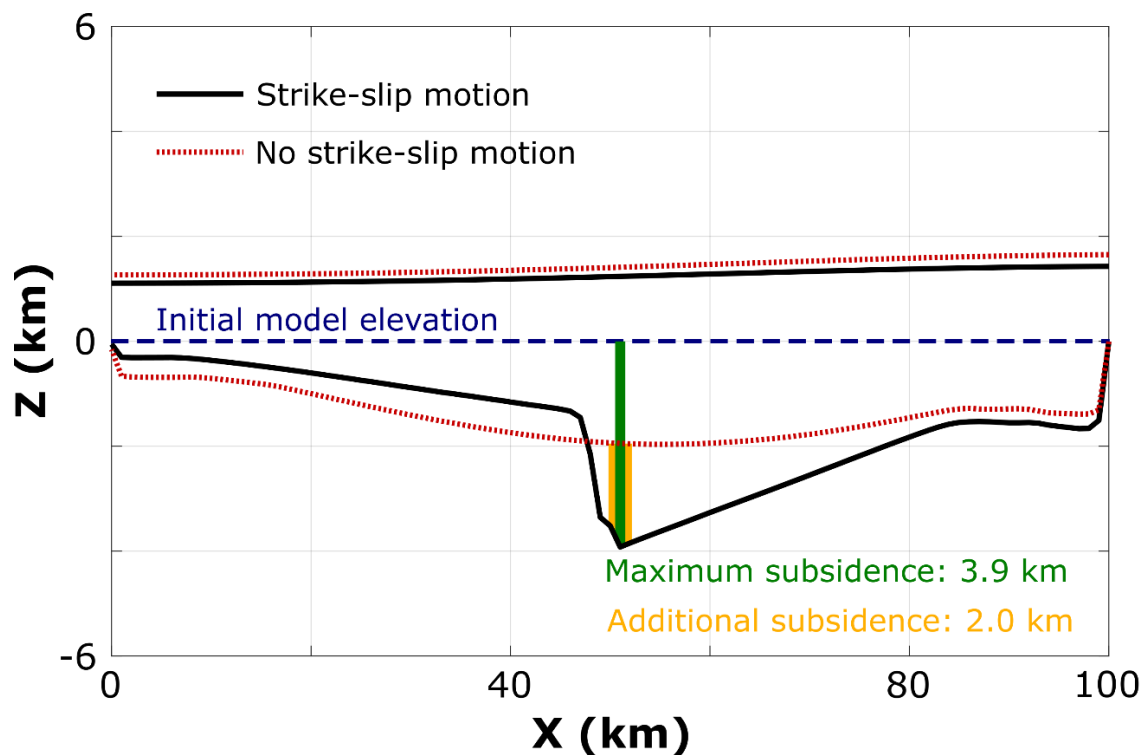
179

180 **Figure S2:** Comparison showing the reference model with A) a 0.2 mm/yr extensional component.

181 B) no extensional component, leading to the formation of a small compressional pop-up in the

182 center.

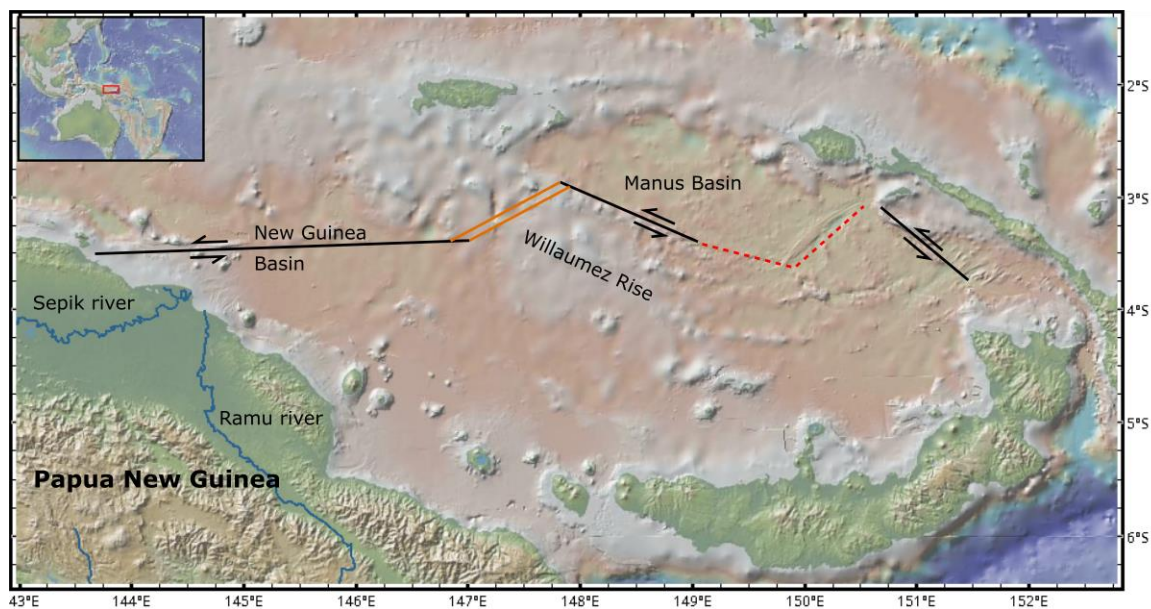
183



184

185 **Figure S3:** Comparison of the FastScape basement and topography from two models runs: The
 186 black curves represent the reference model; the dotted red curves show the reference model without
 187 strike-slip motion. The dashed blue line represents the initial model elevation, the green line
 188 indicates the total subsidence in the reference model with strike-slip motion, and the yellow line
 189 shows the difference in subsidence when comparing models with and without strike-slip motion.
 190 In the case without strike-slip motion, maximum subsidence and basin asymmetry are both greatly
 191 reduced.

192

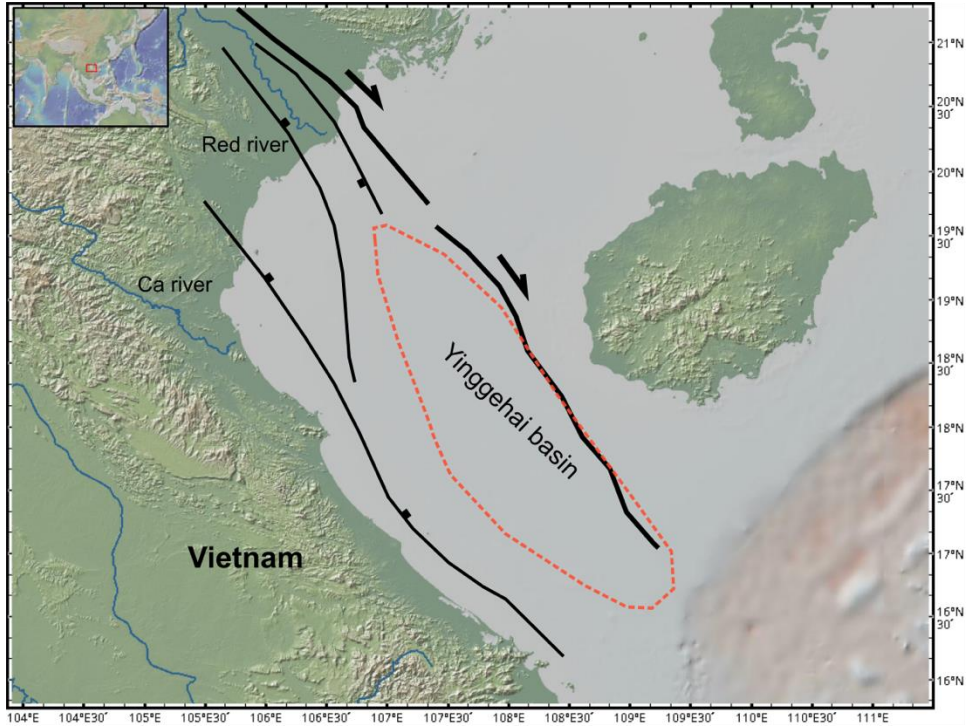


193

194 **Figure S4:** Regional map of the Manus back-arc region, with fault locations based on Fig. 1 in
195 Martinez and Taylor, 1996. Black lines indicate strike-slip faults, parallel orange lines spreading
196 centers, dashed red lines lava fields, and blue lines major rivers. This figure was made using
197 GeoMappApp (www.geomapp.org; Ryan et al., 2009).

198

199



200

201 **Figure S5:** Regional map showing the Red River Fault Zone and location of the Yinggehai basin.

202 Fault locations based on Fig. 10 in Noda, 2013. Black lines show faults, blue lines major rivers,

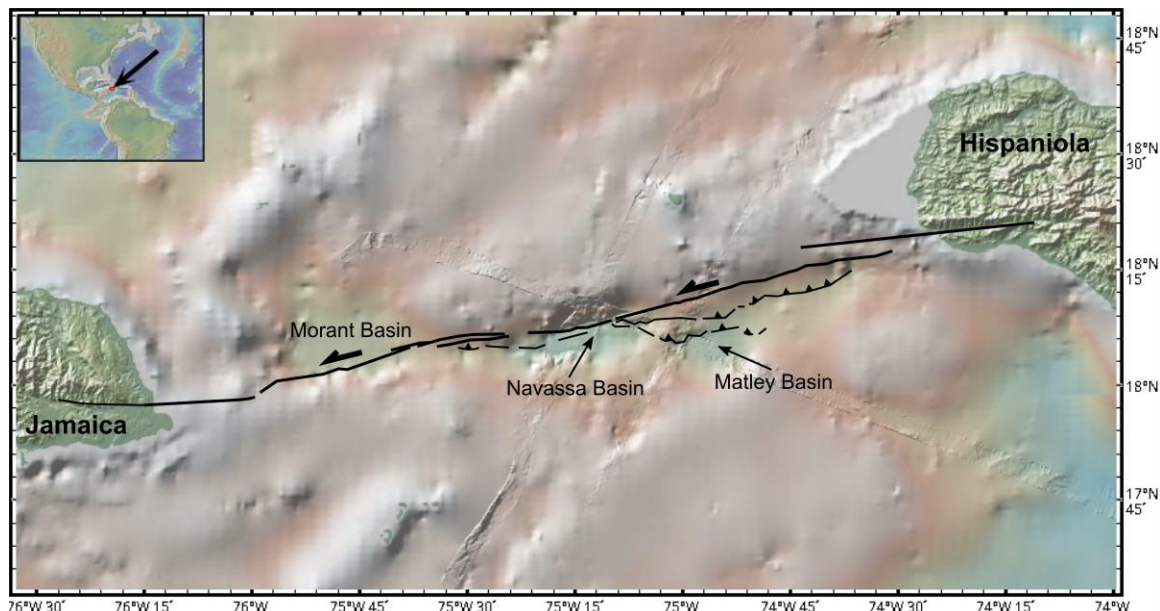
203 and the Yinggehai basin is outlined in the dashed orange circle. This figure was made using

204 GeoMappApp (www.geomapp.org; Ryan et al., 2009).

205

206

207



208
 209 **Figure S6:** Regional map of the Jamaica Passage showing the Navassa strike-slip basin along the
 210 Enriquillo-Plantain-Garden Fault Zone. Fault locations based on Fig. 6 in Corbeau et al., 2016.
 211 This figure was made using GeoMappApp (www.geomapapp.org; Ryan et al., 2009).

212
 213 **Video S1:** Full evolution of the tectonic reference model (Fig. 2C,K,G). Colors represent
 214 composition where tan is sediment, light gray is upper crust, dark gray is lower crust, dark blue is
 215 mantle lithosphere, and light blue is the asthenosphere. The white lines are temperature contours,
 216 gray-scale the strain rate, and arrows indicate the total velocity magnitude.

217
 218 **Video S2:** Evolution of the middle slice of the top 30 km of the reference tectonic model. Colors
 219 represent composition where tan is sediment, light gray is upper crust, dark gray is lower crust,
 220 dark blue is mantle lithosphere, and light blue is the asthenosphere. The white lines are temperature

221 contours, gray-scale the strain rate, and red arrows indicate the subsidence rate (Z velocity) along
 222 the 8 km depth contour.

223

224 **References**

- 225 Bangerth, W., Dannberg, J., Gassmoeller, R., and Heister, T., 2019, ASPECT v2.1.0: Zenodo,
 226 <https://doi.org/10.5281/zenodo.2653531>.
- 227 Braun, J., and Willett, S.D., 2013, A very efficient O(n), implicit and parallel method to solve the
 228 stream power equation governing fluvial incision and landscape evolution: *Geomorphology*,
 229 v. 180–181, p. 170–179, doi:10.1016/j.geomorph.2012.10.008.
- 230 Corbeau, J., Rolandone, F., Leroy, S., Mercier de Lépinay, B., Meyer, B., Ellouz-Zimmermann,
 231 N., and Momplaisir, R., 2016, The northern Caribbean plate boundary in the Jamaica
 232 Passage: Structure and seismic stratigraphy: *Tectonophysics*, v. 675, p. 209–226,
 233 doi:10.1016/j.tecto.2016.03.022.
- 234 Davis, R.O., and Selvadurai, A.P., 2002, *Plasticity and Geomechanics*: Cambridge University
 235 Press.
- 236 Glerum, A., Thieulot, C., Fraters, M., Blom, C., and Spakman, W., 2018, Nonlinear
 237 viscoplasticity in ASPECT: Benchmarking and applications to subduction: *Solid Earth*, v. 9,
 238 p. 267–294, doi:10.5194/se-9-267-2018.
- 239 Heister, T., Dannberg, J., Gasmöller, R., and Bangerth, W., 2017, High Accuracy Mantle
 240 Convection Simulation through Modern Numerical Methods – II: Realistic Models and
 241 Problems.: *Geophysical Journal International*, v. 210, p. 833–851,
 242 doi:doi:10.1093/gji/ggx195.
- 243 Hirth, G., and Kohlstedt, D., 2003, Rheology of the upper mantle and the mantle wedge: a view
 244 from the experimentalists: *Inside the Subduction Factory Geophysical Monograph*
 245 (American Geophysical Union), v. 183.
- 246 Karato, S., and Wu, P., 1993, *Rheology the Upper Mantle : Synthesis*: v. 260.
- 247 Kronbichler, M., Heister, T., and Bangerth, W., 2012, High Accuracy Mantle Convection
 248 Simulation through Modern Numerical Methods.: *Geophysical Journal International*, v. 191,
 249 doi:doi:10.1111/j.1365-246x.2012.05609.x.
- 250 Mahattanachai, T., Morley, C.K., Charusiri, P., and Kanjanapayont, P., 2021, The Andaman
 251 Basin Central Fault Zone, Andaman Sea: Characteristics of a major deepwater strike-slip
 252 fault system in a polyphase rift: *Marine and Petroleum Geology*, p. 104997,
 253 doi:10.1016/j.marpetgeo.2021.104997.
- 254 Martinez, F., and Taylor, B., 1996, Backarc spreading, rifting, and microplate rotation, between
 255 transform faults in the Manus Basin: *Marine Geophysical Researches*, v. 18, p. 203–224,
 256 doi:10.1007/BF00286078.
- 257 Noda, A., 2013, *Strike-Slip Basin – Its Configuration and Sedimentary Facies: Mechanism of*

- 258 Sedimentary Basin Formation - Multidisciplinary Approach on Active Plate Margins,
259 doi:10.5772/56593.
- 260 Rose, I., Buffett, B., and Heister, T., 2017, Stability and Accuracy of Free Surface Time
261 Integration in Viscous Flows.: Physics of the Earth and Planetary Interiors, v. 262, p. 90–
262 100, doi:doi:10.1016/j.pepi.2016.11.007.
- 263 Rouby, D., Braun, J., Robin, C., Dauteuil, O., and Deschamps, F., 2013, Long-term stratigraphic
264 evolution of Atlantic-type passive margins: A numerical approach of interactions between
265 surface processes, flexural isostasy and 3D thermal subsidence: Tectonophysics, v. 604, p.
266 83–103, doi:10.1016/j.tecto.2013.02.003.
- 267 Rutter, E.H., and Brodie, K.H., 2004, Experimental grain size-sensitive flow of hot-pressed
268 Brazilian quartz aggregates: Journal of Structural Geology, v. 26, p. 2011–2023,
269 doi:10.1016/j.jsg.2004.04.006.
- 270 Ryan, W.B.F. et al., 2009, Global Multi-Resolution Topography synthesis: Geochemistry,
271 Geophysics, Geosystems, v. 10, doi:https://doi.org/10.1029/2008GC002332.
- 272 Rybacki, E., Gottschalk, M., Wirth, R., and Dresen, G., 2006, Influence of water fugacity and
273 activation volume on the flow properties of fine-grained anorthite aggregates: Journal of
274 Geophysical Research: Solid Earth, v. 111, doi:10.1029/2005JB003663.
- 275 Sippel, J., Meeßen, C., Cacace, M., Mechie, J., Fishwick, S., Heine, C., Scheck-Wenderoth, M.,
276 and Strecker, M., 2017, The Kenya rift revisited: Insights into lithospheric strength through
277 data-driven 3-D gravity and thermal modelling: Solid Earth, v. 8, p. 45–81, doi:10.5194/se-
278 8-45-2017.
- 279 Turcotte, D.L., and Schubert, G., 2013, Geodynamics: Cambridge University Press.
- 280 Yuan, X.P., Braun, J., Guerit, L., Rouby, D., and Cordonnier, G., 2019a, A New Efficient
281 Method to Solve the Stream Power Law Model Taking Into Account Sediment Deposition:
282 Journal of Geophysical Research: Earth Surface, v. 124, p. 1346–1365,
283 doi:10.1029/2018JF004867.
- 284 Yuan, X.P., Braun, J., Guerit, L., Simon, B., Bovy, B., Rouby, D., Robin, C., and Jiao, R.,
285 2019b, Linking continental erosion to marine sediment transport and deposition: A new
286 implicit and O(N) method for inverse analysis: Earth and Planetary Science Letters, v. 524,
287 p. 115728, doi:10.1016/j.epsl.2019.115728.
- 288